

15 Polarizational Characteristics of the Underwater World

15.1 Underwater Polarized Light Field

In qualitative submarine visual observations down to 15 m Waterman (1954a) found that aquatic animals of the photic zone are surrounded by complex polarization patterns. He used a diving helmet and a hand-held polarization analyser, in which the light first passed through a plate of a uniaxial crystal cut perpendicularly to its optical axis, then through a quarter-wave plate and a linearly polarizing filter. The intensity of unpolarized light passing through this polariscope simply decreases. If the incident light is partially linearly polarized, a brightly coloured interference pattern of concentric, broken rings appears in the polariscope, from which the presence of polarization, the E-vector direction as well as a rough estimate of the degree of linear polarization p can be deduced. The interruptions of the broken rings occur in orthogonal quadrants, and the axis of one of the pairs of these opposed quadrants is parallel to the E-vector of incident light. The intensity of the pattern and the number of concentric rings vary with p . With this polariscope the E-vector direction could be obtained with an accuracy of about $\pm 3^\circ$.

Waterman (1954a) found the following characteristics of the submarine polarized light field (Fig. 15.1): Underwater there are two polarization patterns, one inside and one outside the Snell window, which is visible within the critical angle of the refractive cone.¹ Due to refraction at the water surface, the entire 180°

¹ The boundary of Snell window extends up to $\beta_{SW} = \arctan [n_a / (n_w^2 - n_a^2)^{1/2}] = 48.5^\circ$ measured from the zenith, where $n_a = 1$ and $n_w = 1.333$ are the refractive indices of air and water, respectively. Due to refraction the above-water world visible through the Snell window is distorted (Horváth and Varjú 1991). A point of the firmament with a zenith angle β is apparently seen in direction $\beta^* = \arctan [n_a \sin \beta / (n_w^2 - n_a^2 \sin^2 \beta)^{1/2}]$ from the vertical. The apparent horizon corresponds to the boundary of Snell window. Light from Snell window in shallow waters contains most of the components of the spectrum available to terrestrial animals. Outside Snell window the light from deeper water layers is reflected and it is dim and its spectral range is restricted especially in open waters. At the boundary of Snell window light from near the above-water horizon is split into a rainbow due to dispersion (Jerlov 1976). An above-water object directly overhead suffers

field of view above the water is compressed into a cone with 48.2° half-angle. The polarization pattern of the sky is visible within the Snell window. Chapter 15.3 deals in detail with this pattern. Outside the Snell window is another polarization pattern created by the scattering of sunlight entering the water. Both of these underwater polarization patterns are complex and contain information about the location of the sun. An aquatic animal able to maintain a stable spatial orientation relative to the gravitation and capable of analyzing E-vector direction would have a sun compass available even if the glitter pattern at the depth of the animal would prevent it from seeing the sun directly.

The underwater polarization pattern forms a virtual sphere that surrounds the observer. The highest p occurs in a band along a great circle of this sphere perpendicularly to the refracted sunlight, and the E-vector is always perpendicular to the scattering plane (Fig. 15.1). On cloudy days most of the underwater polarization can be attributed to the scattering of light by water molecules, with little contribution from the polarized skylight.

Small particles suspended in the water scatter most strongly the UV and blue light, while water molecules have absorption bands in the UV and red (Jerlov 1976). Dissolved organic materials absorb UV light extensively, thus the UV light is most attenuated. Attenuation of the blue and red wavelengths can be accredited mostly to absorption by various chlorophylls (Wetzel 1975). p is highest near the water surface (Ivanoff and Waterman 1958b) and decreases rapidly with depth within the first 40 m. The underwater polarization is influenced above a critical depth by the sky as well as the relation between the observer's line of sight and the direction of the underwater rays. Waterman (1954a) hypothesized that under totally overcast skies the E-vector of the underwater polarized light is overall horizontal and the polarization pattern in deep waters is similar to that near the surface on a heavily overcast day.

After the pioneering observations of light polarization in the ocean (Waterman 1954a), a huge amount of experimental (e.g. Ivanoff and Waterman 1958a,b; Waterman and Westell 1956; Timofeeva 1961, 1962, 1969, 1974; Jerlov 1963, 1976; Ivanoff 1974; Loew and McFarland 1990; Novales Flamarique and Hawryshyn 1997a) and theoretical (e.g. Kattawar and Adams 1989; Adams and Kattawar 1993; Kattawar 1994) information has been accumulated about the underwater polarized light field. Submersible point-source scanning polarimeters with different colour filters made possible to collect data in shallow as well as deep marine waters (e.g. Ivanoff and Waterman 1958b; Tyler 1963; Ivanoff 1974).

little refractive distortion when seen from the water, but the image of objects near the horizon is substantially compressed (Horváth and Varjú 1991). When the water is flat, the boundary of Snell window is sharp, and there is a strong contrast between the bright scene above and the darker reflections from deep water. Some plankton-feeding fishes living near the surface have an area of enhanced acuity on that part of their retinae where the boundary of Snell window comes to lie (Munk 1970). One of the two foveae of the compound eye in the water bug *Notonecta glauca* also looks in the direction of the edge of Snell window when the animal rests upside down below the water surface (Schwind 1983b, 1985b).

These results are reviewed and discussed thoroughly by Jerlov (1976). The most complete description of underwater polarization in the visible part of the spectrum combining laboratory and field experiments was given by Timofeeva (1961, 1962, 1969, 1974). In milky solutions in the laboratory, she studied p and α of underwater scattered light as functions of the direction of observation and the azimuth angle of the light source. Ivanoff and Waterman (1958b) as well as Timofeeva (1961) found that p was highest for both milky solutions and ocean waters with the highest absorption and lowest dispersion, regardless of the azimuth angle of the source. Timofeeva (1969, 1974) observed also submarine neutral points in the vertical plane through the observer and the sun. Waterman (1955), Waterman and Westell (1956), Ivanoff and Waterman (1958b) as well as Timofeeva (1969, 1974) found that p decreases with increasing depth, and at a critical depth it reaches a constant maximum value horizontally, when the radiance distribution no longer varies with direction of observation and the downwelling light becomes more vertical. This critical depth depends on the optical properties of the medium and varies from 40 m (Ivanoff and Waterman 1958b) to 200 m (Waterman 1955) in very clear waters. p near the surface of clear water was found to reach 60% depending on the solar azimuth, but at greater depths p dropped to 30% (Ivanoff and Waterman 1958b). Tyler (1963) calculated that even under cloudy skies, p of light in deep water can reach 30-40%. The lowest p occurs approximately at 470 nm, at which light is least attenuated in clear seawater (Hawryshyn 1992).

Lythgoe and Hemmings (1967) reported that when the transmission axis of a linearly polarizing filter was oriented in front of their eyes to exclude the maximally polarized underwater spacelight, the apparent brightness of small fishes (Sparidae and *Atherina*) was reduced less than the background spacelight, and thus fishes had a higher contrast against their background. Furthermore, distant fishes, invisible to the naked eye became visible using the polarizer. Photographing underwater white, black and grey panels through a linear polarizer with two orthogonal transmission axes from different distances and at various depths under cloudless skies, Lythgoe and Hemmings observed that the unobstructed water background has undergone a greater brightness change than the targets. One target, which was brighter than its background with a given orientation of the polarizer, became darker when the polarizer was rotated by 90°. In another experiment, a polarizer was fixed to the outer surface of a diving helmet and oriented to exclude the maximally polarized underwater light. The horizontal distances at which different grey underwater targets just became invisible seen through the helmet with and without the polarizer were measured. Lythgoe and Hemmings found that the polarizer increased or decreased the range at which underwater objects brighter or darker than the water background could be seen. They suggested that polarization sensitivity could enable aquatic animals to see distant objects in clear waters. However, Luria and Kinney (1974) argued that there are so many drawbacks in using polarizers as means of enhancing contrast that underwater vision with polarizers is not reliably superior to vision without them.

The above-mentioned pioneering results of Waterman (1954a) were confirmed also by the polarimetric investigations of Cronin and Shashar (2001). They measured the spatial and temporal variation of the radiance I , p and α of light in clear, tropical marine waters under partly cloudy skies from 350 to 600 nm throughout the day on a coral reef at a depth of 15 m. They used a submersible rotating-analyzer, point-source (15° field-of-view) sequential polarimeter based on a spectrometer with sensitivity in the UV and visible spectral ranges. Light entering a collector aperture and passing through a rotatable linearly polarizing filter was conducted to the spectrometer by a 10 m optical fibre. Polarizational characteristics of the downwelling light were investigated in different directions in the upper hemisphere. They found that both p and α varied only slightly with wavelength. Light was sometimes less polarized in the UV and maximally polarized in the visible range, or *vice versa*, depending on the viewing direction, solar elevation and sky cloudyness. Thus, they could find no particular optimum wavelength range for polarization-sensitive photoreceptors of underwater animals. p was always less than 50%.

The complex underwater intensity and polarization patterns are modified by spatio-temporal variations of light distribution due to surface waves (Jelley 1989), which focus sunlight at different depths depending on the wavelength. Surface ripples focus light at depths of few centimetres, longer waves at greater depths (Schenck 1957). Wave-focusing causes flicker, the frequency of which decreases with increasing depth.

15.2 Underwater Polarized UV Light and the UV Polarization Sensitivity in Fishes

The ability to utilize UV light (UV-A: $320 \text{ nm} < \lambda < 400 \text{ nm}$) is widespread among terrestrial and aquatic arthropods, fresh- and saltwater fishes (e.g. Tové 1995), reptiles (e.g. Fleishman et al. 1993), birds (e.g. Bennett et al. 1996) and some amphibians and tiny mammals (e.g. Goldsmith 1994). In fishes, UV sensitivity can persist throughout most of the animal's lifetime as in the goldfish *Carassius auratus* (Neumeyer 1985; Fratzer et al. 1994), or it may be restricted primarily to specific periods such as the presmolting and reproductive stages of salmon (Beaudet et al. 1993; Novalés Flamarique and Hawryshyn 1996; Beaudet et al. 1997).

There are several possible functions of UV sensitivity in fishes, e.g. contrast enhancement of planktonic targets that absorb or scatter UV light differently from the water background (Loew et al. 1993; Browman et al. 1994), or reflective communication, especially among schooling fishes (e.g. Denton and Rowe 1994), or polarization sensitivity (e.g. Coughlin and Hawryshyn 1995). Because shorter wavelengths are scattered most strongly in water (McFarland and Munz 1975; Novalés Flamarique and Hawryshyn 1997a) and UV cones are primarily located in areas of low photoreceptor density of the retinae in various fishes (e.g. Beaudet et al. 1997), furthermore since involving the near-UV part of the spectrum to

vision enhances the chromatic aberration of the dioptric apparatus (e.g. Sivak and Mandelman 1982), it is believed that UV sensitivity does not enhance the visual acuity in fishes in contrast to sensitivity in other parts of the spectrum.

The UV-sensitive neural pathways are usually polarization sensitive in fishes (e.g. Hawryshyn and McFarland 1987; Parkyn and Hawryshyn 1993; Coughlin and Hawryshyn 1995). This is not always the case for the neural mechanisms mediating sensitivity in other parts of the spectrum, e.g. the blue cones in certain cyprinids and salmonids (Hawryshyn and McFarland 1987; Coughlin and Hawryshyn 1995) and the green and red cones in green sunfishes (Cameron and Pugh 1991; Novales Flamarique and Hawryshyn 1997b) are polarization-blind.

Studying the photic environment of a salmonid nursery lake, Novales Flamarique et al. (1992) found that although strongest attenuation of light occurred in the UV, there was enough light to stimulate all UV-sensitive photoreceptors in juvenile salmonid retinae from a depth of 18 m to the surface. This depth restriction may be linked to the observed salmonid movements close to the surface during crepuscular periods, when the relative proportion of UV, blue and green light with respect to the entire spectrum was maximal while that of red light was minimal. UV polarization sensitivity may enable juvenile salmonids to detect zooplankton which absorb and polarize UV light due to their pigments and birefringent skeletons.

Novales Flamarique and Hawryshyn (1997a) measured the spectral distribution of the underwater polarized light field at a depth of 4 m under clear skies in the upper photic zone of meso-eutrophic waters, i.e. blue-green waters containing medium to high chlorophyll-A concentrations. They found that the maximum degree of polarization p_{max} during the day was 35-40%, but at dawn and dusk it increased to 67%. The reason for this is that during the crepuscular period underwater polarization is mainly determined by the incident light from the sky, which is maximally polarized when the sun is on the horizon. At dawn and dusk also the relative contribution of blue and UV wavelengths to the total spectrum increased. In blue oligotrophic waters, where smaller particles create higher Rayleigh scattering, $p_{max} = 60\%$ was measured for daylight hours by Waterman and Westell (1956) as well as Ivanoff and Waterman (1958b). Electrophysiological recordings from the optic nerve of young rainbow trouts (*Oncorhynchus mykiss*) stimulated by partially linearly polarized light with spectral characteristics mimicking that of the natural underwater light field indicated that the threshold of p for detection of polarization is between 63% and 72%. This threshold value is very high compared with those as low as 5-10% in field crickets and honeybees. These physiological findings suggest that the use of underwater polarization by rainbow trouts should be restricted to crepuscular periods and only to regions near (< 7 m) the water surface.

15.3 Underwater Refraction-Polarization Patterns of Skylight Perceived by Aquatic Animals through the Snell Window of the Flat Water Surface

In this chapter we give a quantitative account of the physics of repolarization of skylight transmitted through the flat water surface on the basis of Horváth and Varjú (1995). The polarizational characteristics of skylight are described by the single-scattering Rayleigh model (Coulson 1988). It is assumed that the air-water interface is without ripples and the refraction polarization of light at the water surface is governed by the Fresnel formulae (Guenther 1990). The contribution of underwater polarization due to scattering in water is neglected. This approximation is reasonable if the underwater observer is near the water surface.

15.3.1 Refraction-Polarization Ellipses, Degree and Angle of Linear Polarization of Refracted Light

In Fig. 15.2 the amplitude transmission coefficients σ_{par} and σ_{perp} for parallel and perpendicular E-vector of totally linearly polarized incident light are shown as a function of the incident angle θ_i at the air-water interface. The vertically polarized light is slightly less attenuated than the horizontally polarized light at all θ_i except $\theta_i = 0^\circ$ and $\theta_i = 90^\circ$. When the E-vector direction of totally polarized light is oblique, it can be decomposed into a horizontally and a vertically polarized component both of which oscillate coherently. Since the vertical component is less attenuated, the plane of polarization of the sum of the components will become more vertical, so that the E-vector rotates towards the vertical after refraction if $\theta_i \neq 0^\circ$ and $\theta_i \neq 90^\circ$.

The refractive indices of air and water vary slightly with the wavelength of light, such that less light is transmitted in the UV than in the visible range of the spectrum (Guenther 1990). This dispersion, however, is not strong. The refractive index of red (656.3 nm) light amounts to 1.3312, that of UV (308.2 nm) light to 1.3567. Therefore one can omit the spectral character of skylight and use in the calculations the refractive indices $n_{air} = 1$ and $n_{water} = 1.333$, that correspond to wavelengths in the middle range (587.6 nm) of the visible spectrum.

After refraction at the water surface unpolarized incident light becomes partially linearly polarized with vertical E-vector at any θ_i . In Figs. 15.3A,B the shape of the refraction-polarization ellipses (RPE's) are depicted as a function of θ_i of unpolarized incoming light. Figures 15.3C,D show the degree of linear polarization p_r of refracted light and the transmissivity T of the water surface for unpolarized incident light versus θ_i . The greater the θ_i , the larger the p_r of refracted light (Fig. 15.3C). As θ_i increases, the size of the RPE decreases (Figs. 15.3A,B) due to the decrease of T (Fig. 15.3D). Since $\sigma_{par} \leq \sigma_{perp}$ (Fig. 15.2) the RPE for unpolarized incident light is slightly elongated (Figs. 15.3A,B).

If the incident light is partially linearly polarized, as is skylight, the spatial distribution of the incident E-vectors is characterized by a polarization ellipse. In this case the influence of refraction on the unpolarized and totally polarized parts of incident light can be superimposed. The unpolarized component is partially converted into vertically polarized light (Fig. 15.3) and the totally polarized part rotates its plane of oscillation towards the vertical, unless its E-vector is horizontal or vertical. Figure 15.4 illustrates the RPE's, p_r and α_r of refracted light as a function of θ_i for $p_i = 0.5$ and different α_i of the incident light. Since the vertical component of the incident electric field vectors is less attenuated than the horizontal one (Fig. 15.2), the RPE rotates towards the vertical, i.e. α_r decreases as θ_i increases, whenever the incident E-vector is oblique relative to the water surface (Figs. 15.4B,C), but not when the incident E-vector is vertical (Fig. 15.4A) or horizontal (Fig. 15.4D). Figure 15.4 also demonstrates that p_r of refracted light increases with increasing θ_i when α_i is less than 30° (Figs. 15.4A,B). The opposite is true when α_i is larger than 60° (Figs. 15.4C,D).

15.3.2 Refraction-Polarization Patterns of Skylight Visible Through Snell Window Versus the Solar Zenith Angle

One of the possible ways of displaying the celestial polarization pattern is to represent the distribution of polarization ellipses of skylight in two dimensions. This is shown in Fig. 15.5 for four different solar zenith angles. Figures 15.6A-D show the corresponding patterns of RPE's, and Fig. 15.6E represents the refraction-polarization pattern calculated for unpolarized light of a totally overcast sky. Spectral and intensity differences in skylight were not taken into consideration.

Another way of displaying is to plot lines along which p and α of incident and refracted skylight are constant. For a better visualization we shaded the areas between neighbouring isolines with different grey tones. Figure 15.7 shows the distribution of p of skylight for different solar zenith angles θ_s . Figures 15.8A-D demonstrate the corresponding patterns after refraction at the flat water surface under clear skies. Figure 15.8E was calculated for unpolarized light of an overcast sky. In Fig. 15.9 some contour lines of equal p of skylight refracted within the Snell window are shown for different θ_s to represent the neutral points near the apparent sun and antisen. In Fig. 15.7 the celestial neutral points coincide with the solar and antisolar points. Figure 15.9 demonstrates, however, that the neutral points within the Snell window do not correspond to the position of the apparent sun and antisen but they are shifted further away from the latter, except when the sun is at the zenith (Fig. 15.9A).

In addition to the distortion of the contour lines of p by refraction, there are also some qualitative differences between the celestial polarization patterns in Fig. 15.7 and the corresponding refraction-polarization patterns in Figs. 15.8 and 15.9. When the sun approaches the zenith, the band of maximum p of the firmament with nearly horizontally polarized skylight lies near the horizon (Figs. 15.7A,B).

Since p of refracted light for nearly horizontally polarized incoming light decreases with increasing incident angle (Figs. 15.4C,D), the contour lines of equal p of refracted light move further away from the solar point, i.e. they are shifted towards the boundary of Snell window (Figs. 15.8A,B and 15.9A,B). However, when the sun approaches the horizon, the celestial maximally polarized band with nearly vertically polarized skylight lies near the zenith (Figs. 15.7C,D). Since p of refracted light for nearly vertically polarized incoming light increases with increasing incident angle (Figs. 15.4A,B), the contour lines of equal p of refracted light are shifted towards the solar and antisolar points (Figs. 15.8C,D and 15.9C,D). This results in two strongly polarized wedge-shaped patches near the boundary of Snell window perpendicularly to the solar meridian (Figs. 15.8C,D and 15.9C,D).

The α -patterns of skylight are shown in Fig. 15.10 as a function of the solar zenith angle θ_s . Since all celestial E-vectors are directed horizontally when the sun is at the zenith, the pattern in Fig. 15.10A is uniformly dark blue. The corresponding patterns of refracted skylight are shown in Fig. 15.11. The E-vector of refracted light is also always horizontal when the sun is at the zenith, the pattern in Fig. 15.11A is, therefore, also homogeneously black. In this two-dimensional representation the contour lines of equal α in Figs. 15.10B-D converge. One of the celestial points of convergence is always the zenith, and the other ones are the solar and antisolar points (Figs. 15.10B-D).

The most prominent difference between the patterns in Figs. 15.10 and 15.11 is that the point of convergence at the sun (Fig. 15.10B) is split into two points of convergence positioned around the apparent sun along the solar meridian (Fig. 15.11B). The skylight from the solar meridian is always horizontally polarized and its p decreases gradually towards the sun, where it is unpolarized. The unpolarized direct sunlight becomes slightly vertically polarized after refraction (Fig. 15.3). As the direction of view moves off the sun, p of skylight gradually increases along the solar meridian (Fig. 15.7). If p of this light is low, i.e. the angular distance from the sun is short, then the refracted light also becomes partially vertically polarized. However, if it is polarized over a certain threshold, the refracted light remains partially horizontally polarized but its p is slightly reduced (Fig. 15.4D). Hence there are two distinct points along the solar meridian and near the apparent sun where the direction of polarization of refracted skylight switches from vertical to horizontal. These points coincide with the two points of convergence around the apparent sun (Fig. 15.11B) and they constitute the two neutral points there (Fig. 15.9B).

In Figs. 15.12A-D the two-dimensional patterns of transmissivity T of the flat air-water interface are shown for different θ_s . The T -pattern in Fig. 15.12E is computed for unpolarized light of an overcast sky. These patterns have in all cases approximately a cylindrical symmetry for $T < 95\%$. The T -pattern calculated for clear sky with the sun at the zenith (Fig. 15.12A) and that for unpolarized skylight (Fig. 15.12E) have an exact cylindrical symmetry. As the sun approaches the horizon, the contour lines of equal T gradually become elongated, they are flattened perpendicularly to the solar meridian. The patches in Figs. 15.12C,D represent those regions where $T > 98\%$. These bright patches correspond to the

two dark patches of the water surface visible from air, where the surface is particularly transparent (see Figs. 11.8C,D and 12.7D,G,J).

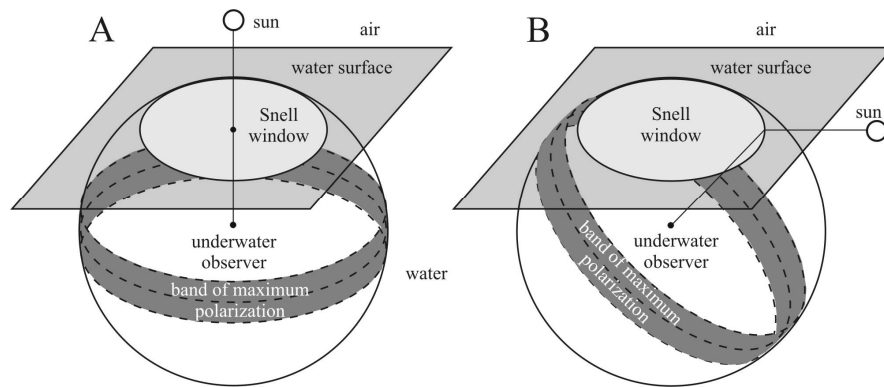


Fig. 15.1. The underwater polarization pattern forms a virtual sphere that surrounds the observer. The distribution of polarization underwater depends on the position of the sun and the relative stillness of the water surface. The highest degree of linear polarization occurs in a band that runs along a great circle of this sphere perpendicularly to the refracted sunlight, and the E-vector is always perpendicular to the scattering plane. (After Fig. 3 of Hawryshyn 1992, p. 167).

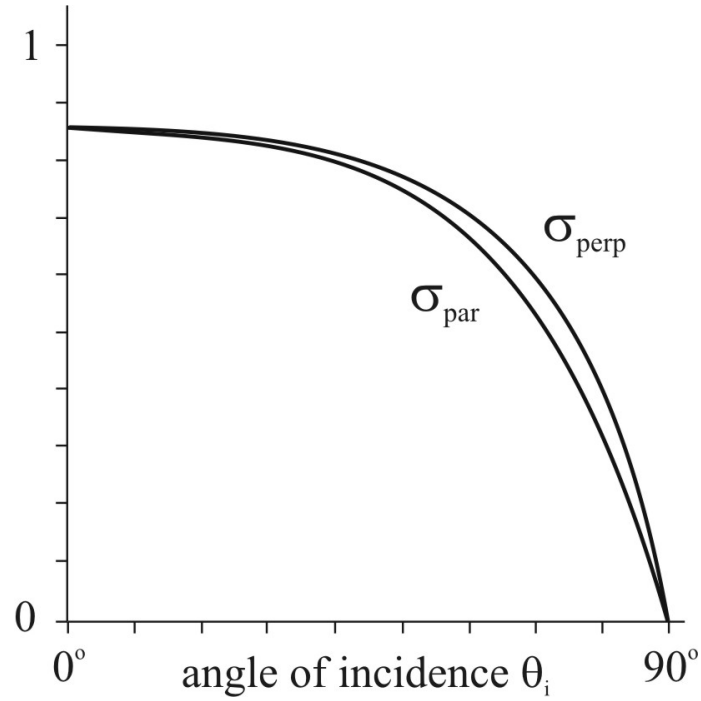


Fig. 15.2. Amplitude transmission coefficients σ_{par} and σ_{perp} as a function of the incident angle θ_i measured from the vertical for parallel and perpendicular E-vector of totally linearly polarized incoming light with respect to the water surface calculated for the flat air-water interface with $n_{air} = 1$ and $n_{water} = 1.333$. (After Fig. 1 of Horváth and Varjú 1995, p. 1653).

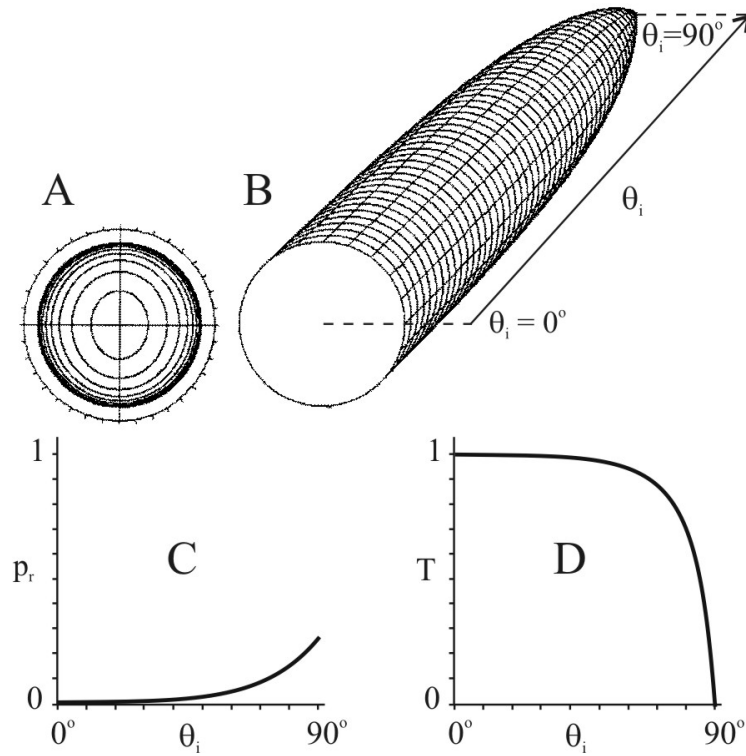


Fig. 15.3. A: Refraction-polarization ellipses for unpolarized ($p_i = 0$) incident light as a function of the incident angle θ_i increasing from 0° to 90° in steps of $\Delta\theta_i = 9^\circ$ from the centre towards the periphery. The outermost circle with a graduated scale shows the spatial distribution of the electric field vector of unpolarized light. B: Representation of the refraction-polarization ellipses versus θ_i in a perspective view. C, D: Degree of linear polarization p_r of refracted light, and transmissivity T of the flat air-water interface versus θ_i for unpolarized incoming light. (After Fig. 2 of Horváth and Varjú 1995, p. 1653).

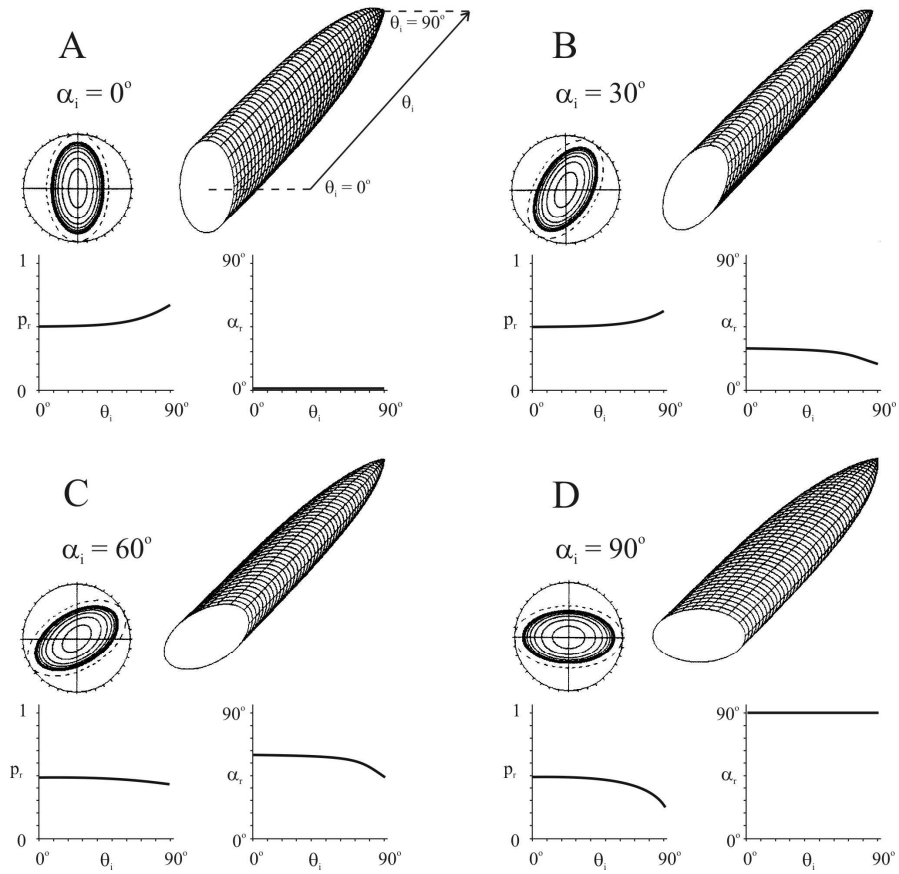


Fig. 15.4. Refraction-polarization ellipses, degree p_r , and angle α_r , of linear polarization of refracted light as a function of the incident angle θ_i of partially linearly polarized incident light with $p_i = 0.5$ for different α_i measured from the vertical. The dashed ellipses illustrate the polarization ellipses of incident light. (After Fig. 3 of Horváth and Varjú 1995, p. 1654).

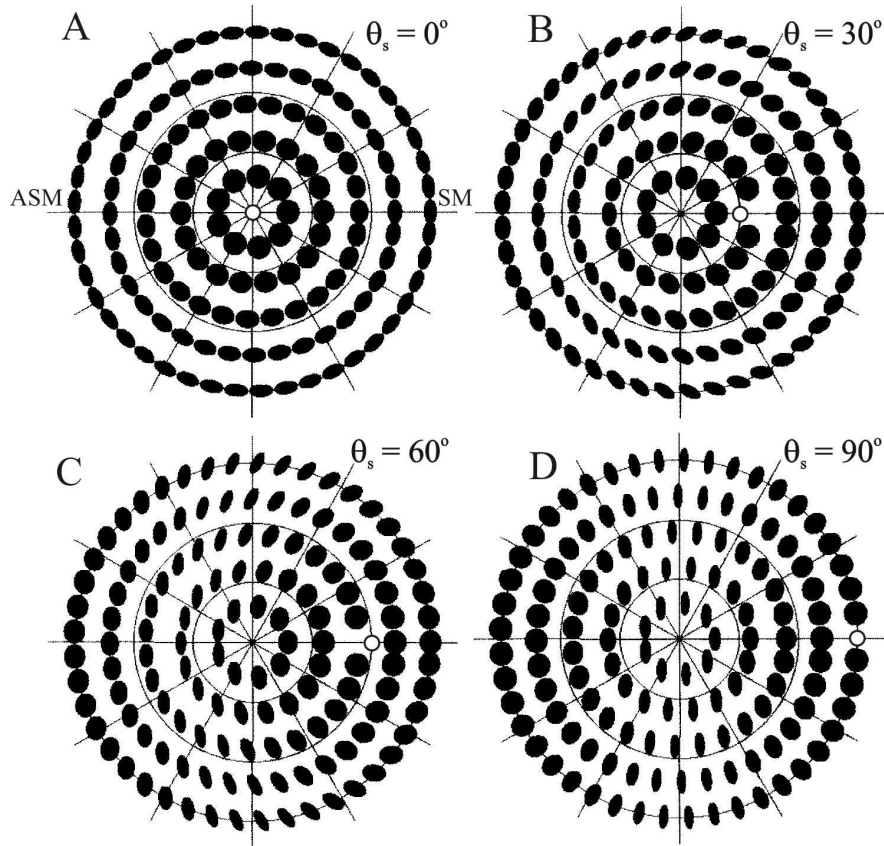


Fig. 15.5. Two-dimensional representation of the pattern of polarization ellipses of skylight for different solar zenith angles θ_s . The polar-coordinate system represents the celestial hemisphere. The zenith is at the centre, the sun is indicated by a dot, the horizon is the outermost circle; SM: solar meridian; ASM: antisolar meridian. The direction of observation θ from the zenith changes radially (zenith: $\theta_z = 0^\circ$, horizon: $\theta_h = 90^\circ$). The azimuth angle φ is the angle between the solar meridian SM and the meridian of the point observed (solar meridian: $\varphi_{SM} = 0^\circ$, antisolar meridian: $\varphi_{ASM} = 180^\circ$). (After Fig. 4 of Horváth and Varjú 1995, p. 1655).

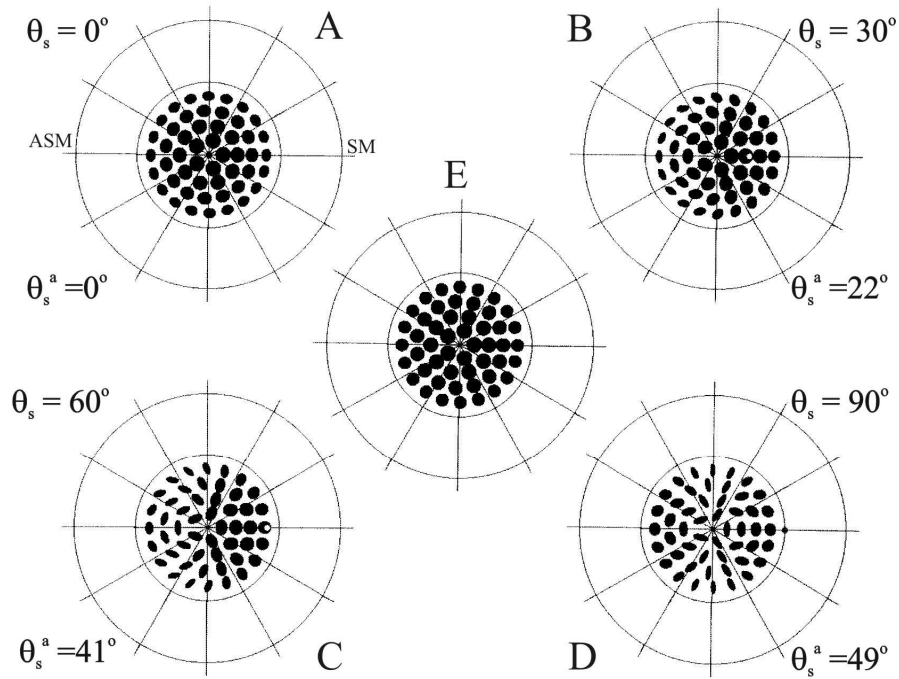


Fig. 15.6. A-D: Two-dimensional representation of the pattern of refraction-polarization ellipses of skylight visible from water through Snell window of the flat water surface for different solar zenith angles θ_s and for the corresponding apparent zenith angles θ_s^a within the Snell window. The large circles correspond to the above-water horizon, the smaller ones represent the boundary of Snell window with an angular diameter of 97° . Other conventions as in Fig. 15.5. E: Pattern of the refraction-polarization ellipses within Snell window for unpolarized light from a totally overcast sky. (After Fig. 5 of Horváth and Varjú 1995, p. 1656).

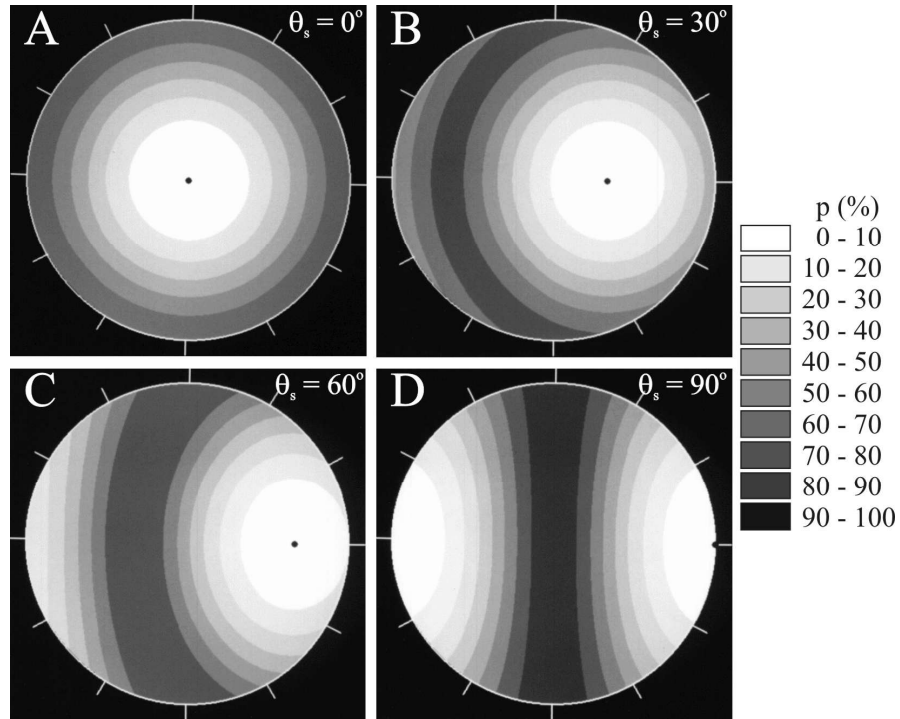


Fig. 15.7. Two-dimensional pattern of the degree of linear polarization p of skylight for different solar zenith angles θ_s . Other conventions and parameters as in Fig. 15.5. (After Fig. 6 of Horváth and Varjú 1995, p. 1657).

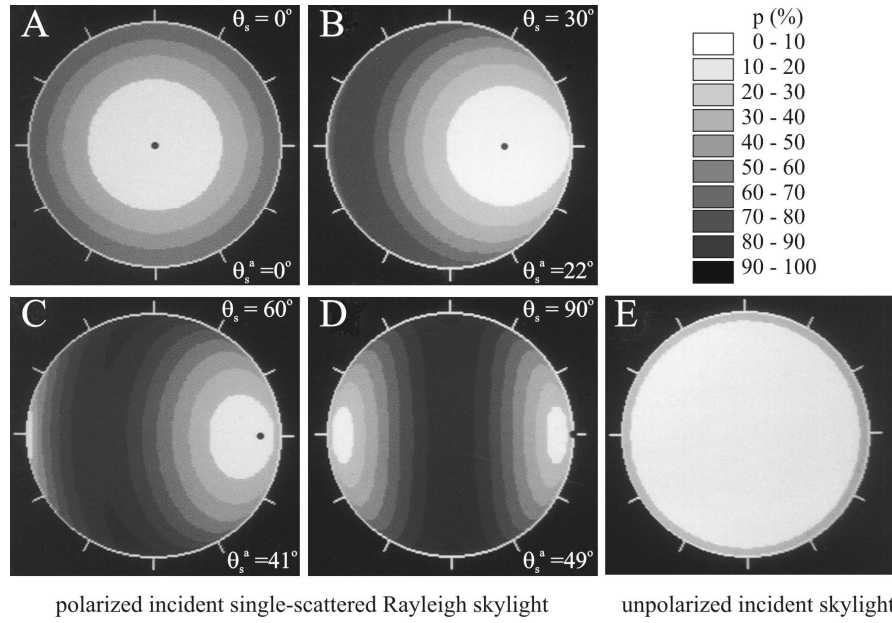


Fig. 15.8. A-D: Pattern of the degree of linear polarization p of skylight refracted within Snell window of the flat water surface under clear skies for different solar zenith angles θ_s and for the corresponding apparent zenith angles θ_s^a within the Snell window. θ_s and θ_s^a as in Fig. 15.6. E: As A-D for unpolarized light from a totally overcast sky. The outermost circles represent the boundary of Snell window. (After Fig. 7 of Horváth and Varjú 1995, p. 1658).

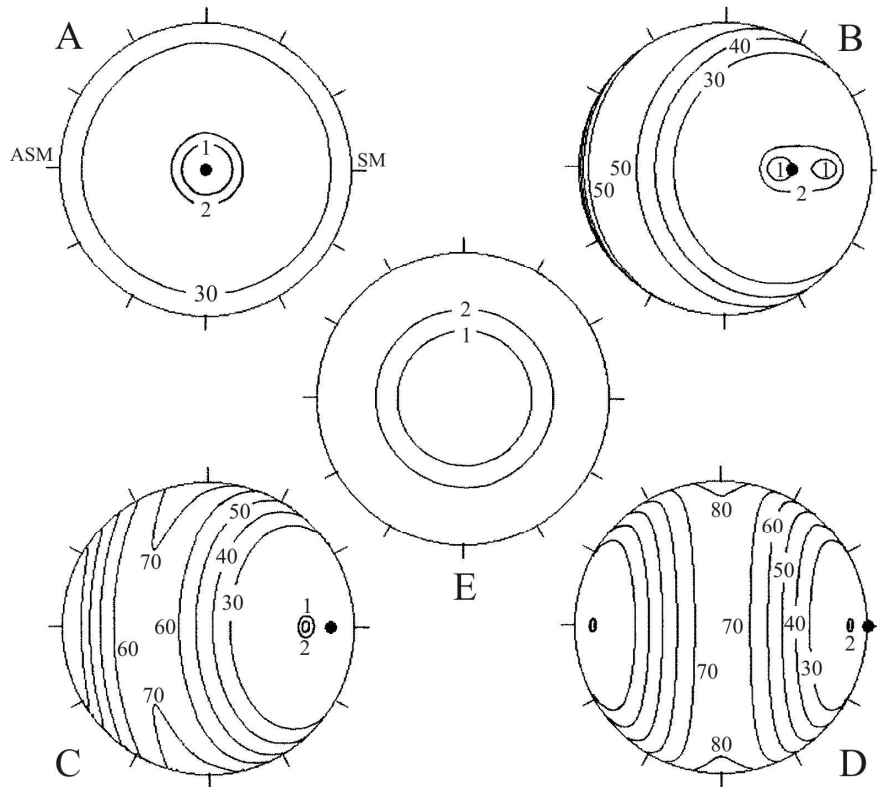


Fig. 15.9. A-D: Contour lines of equal degree of linear polarization p of skylight refracted within the Snell window of the flat water surface for different solar zenith angles θ_s and for the corresponding apparent zenith angles θ_s^a within the Snell window. θ_s and θ_s^a as in Fig. 15.6. E: As A-D for unpolarized light from a totally overcast sky. The apparent position of the sun is indicated by a dot. The outermost circles represent the boundary of Snell window. The p -values of refracted light in % are indicated at the corresponding contour lines. (After Fig. 8 of Horváth and Varjú 1995, p. 1659).

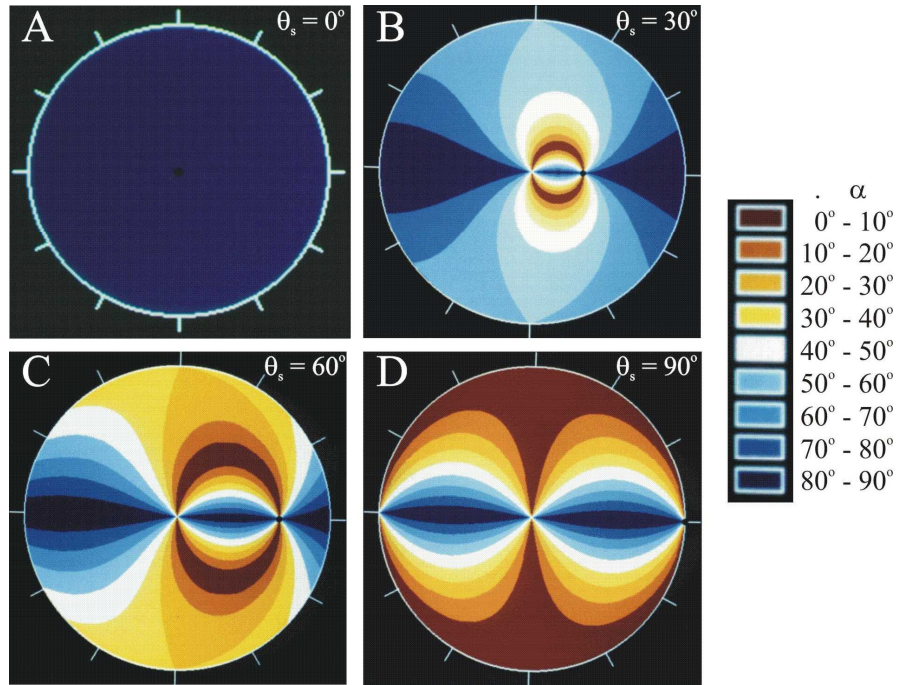


Fig. 15.10. As Fig. 15.7 for the angle of polarization α of skylight measured from the meridian of the point observed in the clear sky. Since all E-vectors of the celestial polarization pattern are horizontal when the sun is at the zenith, pattern A is homogeneous dark blue. (After Fig. 9 of Horváth and Varjú 1995, p. 1660).

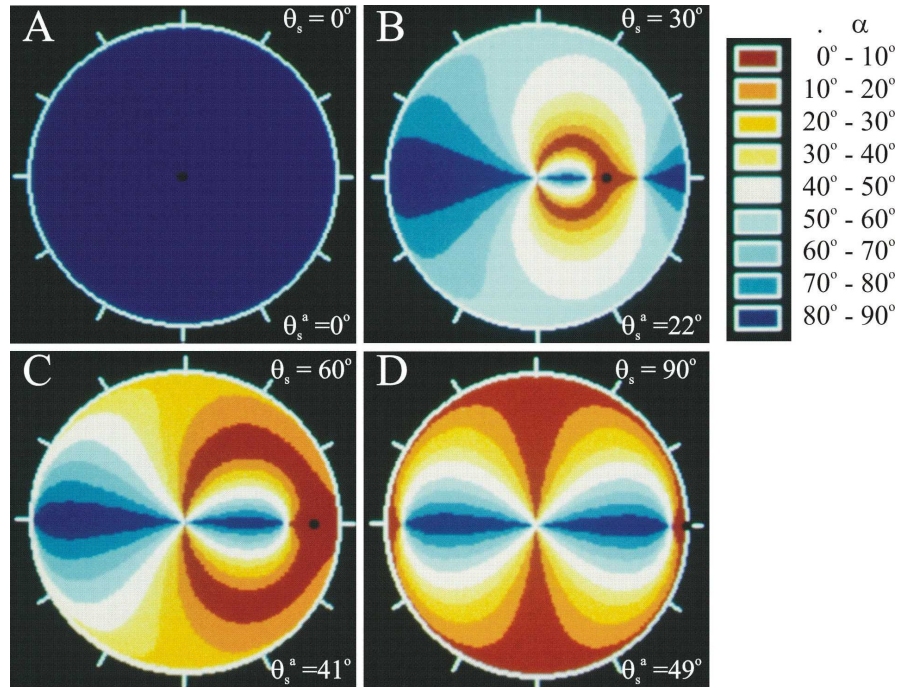


Fig. 15.11. Patterns of the angle of polarization α of refracted skylight within Snell window of the flat water surface under clear skies for different solar zenith angles θ_s . α is measured from the meridian of the celestial point observed through the Snell window. Since all refracted E-vectors are horizontal when the sun is at the zenith, pattern A is homogeneous dark blue. The outermost circles represent the boundary of Snell window. (After Fig. 10 of Horváth and Varjú 1995, p. 1661).

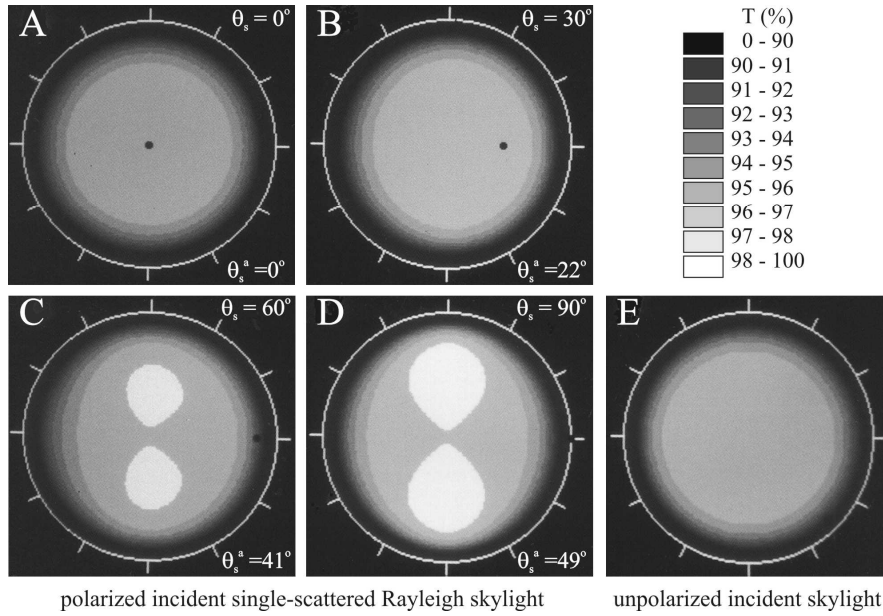


Fig. 15.12. A-D: Patterns of transmissivity T of the flat air-water interface under clear skies visible from water through the Snell window for different solar zenith angles θ_s . E: As A-D for unpolarized light of a totally overcast sky. In patterns C and D the two bright patches show the regions of Snell window where $T > 98\%$. The outermost circles represent the boundary of Snell window. (After Fig. 11 of Horváth and Varjú 1995, p. 1662).